AIAA SciTech Forum
11–15 & 19–21 January 2021, VIRTUAL EVENT
AIAA Scitech 2021 Forum

10.2514/6.2021-1732

Numerical Investigation of Longitudinal Static Stability of a High-Speed Tandem-Wing VTOL Vehicle Using CoFlow Jet Airfoil

Jeremy Boling*,Ge-Cheng Zha†
Department of Mechanical and Aerospace Engineering
University of Miami, Coral Gables, Florida 33124
E-mail: gzha@miami.edu

This paper numerically investigates the longitudinal static stability of a tandem-wing CoFlow Jet VTOL (CFJ-VTOL) aircraft concept with high speed cruise Mach number of 0.6. A tandem wing configuration is desirable for VTOL aircraft since it provides a high hovering stability with dual lifting vectors. However, it brings challenges for cruise to maintain high efficiency and high longitudinal static stability. The design uses CoFlow Jet (CFJ) active flow control wings with propellers mounted above the suction surfaces. The wings are stacked using CFJ-NACA-6415 airfoil. This system allows reduced power consumption at takeoff while providing a benefit to efficiency at cruise. A previous study of the this CFJ-VTOL aircraft concept at cruise shows a high efficiency at Mach 0.6. However, the high efficiency configuration often has a conflict with a high longitudinal static stability. This study conducts trade studies to optimize the efficiency with sufficient longitudinal static stability, including varying the streamwise spacing of the wings, their individual aspect ratios and incidence angles, and the jet intensity of the CFJ system. In order to achieve longitudinal stability, the front wing lift slope needs to be shallower than that of the rear wing so that the front wing is less sensitive to the variation of angle of attack than the rear wing. This is achieved by having the aspect ratio of the front wing to be 25% of the rear wing. The front wing incidence angle is 3° and the rear wing is 0°. The large contribution of the fuselage toward the overall pitching moment requires the fuselage incidence angle to be 5° at cruise, which allows a positive pitching moment at $\alpha = -5^\circ$ when the lift coefficient is about zero. This configuration fulfills the requirement of $C_{M\alpha} < 0$ for the range of $-5^\circ \leq \alpha \leq 2^\circ$. The tandem wing VTOL vehicle achieves an excellent aerodynamic efficiency of 15.3 at Mach 0.6.

Nomenclature

V	Flow Velocity
ρ	Air Density
α, AoA	Angle of Attack
$\dot{m}$	Mass Flow Rate
M	Mach Number
M_i	Isentropic Mach Number
Re	Reynolds Number
L	Aerodynamics Lift
D	Aerodynamic Drag
p	Static Pressure
p_0	Total Pressure
η	Pumping Power
q_∞	Freestream Dynamic Head, $\frac{1}{2}\rho_\infty {V_\infty}^2$

*PhD Candidate
†Professor, AIAA Associate Fellow

C_L	Lift Coefficient, $\frac{L}{q_\infty S}$
C_{L_α}	Slope of Lift Coefficient vs Angle of Attack
C_{LMAX}	Maximum Lift Coefficient
C_D	Drag Coefficient, $\frac{D}{q_\infty S}$
C_M	Moment Coefficient, $\frac{M}{q_\infty S c}$
C_{M_α}	Slope of Moment Coefficient vs Angle of Attack
C_p	Pressure Coefficient, $\frac{p-p_\infty}{q_\infty}$
C_μ	Jet Momentum Coefficient, $\frac{\dot{m}_j v_j}{q_\infty S}$
$(\frac{L}{D})$	Conventional Aerodynamic Efficiency
P_c	Power Coefficient, $\frac{L}{q_\infty S V_\infty}$
$(\frac{L}{D})_c$	Corrected Aerodynamic Efficiency for CFJ Airfoil, $\frac{L}{D+P/V_\infty} = \frac{C_L}{C_D+P_c}$
$(\frac{C_L^2}{C_D})$	Productivity Efficiency Coefficient
$(\frac{C_L^2}{C_D})_c$	Corrected Productivity Efficiency Coefficient for CFJ Airfoil
∞	Free Stream Conditions

I. Introduction

I.A. Longitudinal Static Stability

A tandem wing configuration is desirable for vertical takeoff/landing aircraft (VTOL) aircraft since it provides a high hovering stability with dual lifting vectors. The advantages of tandem wing configuration include: 1) generating lift from two lifting vectors for hovering with high stability; 2) high structure strength and high aircraft maneuverability; 3) more compact size. But the tandem wings may suffer some aerodynamic efficiency loss due to reduced aspect ratio and wing-wing interaction. It also brings challenges for cruise to maintain high efficiency and high longitudinal static stability for the same configuration.

The tandem-wing designs can eschew a horizontal tail, as the lifting surfaces are large enough to provide lift, trim and static stability. The lack of a horizontal tail may also benefit efficiency in the form of less induced drag. The loss of the horizontal tail means the dual wing design takes on the responsibility of generating the moments necessary for stability and trim. Tandem wings are shown both numerically and experimentally to have an advantage in total drag compared to a traditional single wing and tail design. These differences in design philosophy mean a difference in obtaining efficiency and stability. It is shown that in order for some tandem wing aircraft to be longitudinally stable, the static margin has to be greater than single wing designs. Placing the center of gravity far enough forward for stability could be in conflict with the optimal lift-to-drag ratio.

Static stabilities are essential when considering the aerodynamic design of aircraft. They allow the aircraft to produce an opposing force to counteract a disturbance in level, trimmed flight. When describing static stability, one of the key areas is longitudinal static stability. The aircraft is considered stable when the change in pitching moment as a function of angle of attack is negative. For example, if the aircraft is given an instantaneously higher angle of attack due to a disturbance, a stable aircraft should produce a nose down pitching moment.

For an aircraft to be longitudinally stable, the following conditions must be met:[1]

$$C_{M_\alpha} < 0, C_{M_{L=0}} > 0 \tag{1}$$

$$C_{L_\alpha} > 0 \tag{2}$$

This means the lift coefficient at the zero lift angle of attack must be positive, while the pitching moment coefficient must have a negative slope. For a tandem wing configuration to satisfy these requirements, the design consideration is different from conventional configuration with a wing and horizontal tail control surface. This paper is to address this issue, in particular for a tandem wing configuration with coflow jet active flow control.

I.B. CFJ Active Flow Control

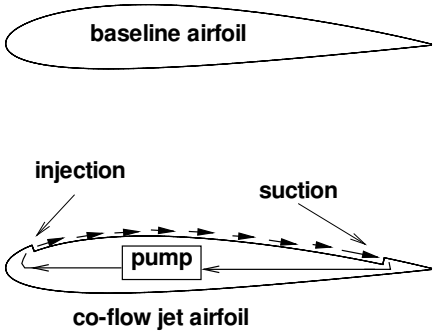

Figure 1: The CFJ airfoil control volume schematic.

The Co-Flow Jet airfoil is a zero-net mass-flux(ZNMF) active flow control technique developed by Zha et al.[2–15] Using this technique applied to a traditional airfoil provides the ability to increase lift and aerodynamic efficiency at low energy expenditure. This low energy expenditure is resulted from placing an injection slot near the leading edge and a suction slot near the trailing edge. Flow is injected near the suction peak and sucked in at a position of higher pressure. Applied to an airfoil, these locations resemble Figure 1. With the help of a pumping system inside the airfoil, a small amount of air from near the trailing edge is sucked in and the energized flow is injected near leading edge in a direction tangent to the main flow. The process does not add any mass flow and hence is a ZNMF system. This technique works by energizing the boundary layer and hence increasing circulation, augmenting stall angle of attack while decreasing pressure drag due to enhanced leading edge suction and filled wake.

I.C. CFJ-VTOL Aircraft Concept

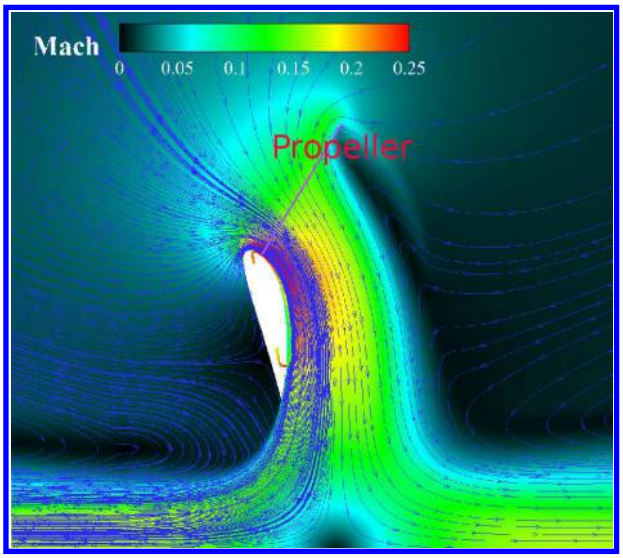

Figure 2: Zoomed in Mach contours of the CFJ airfoil with a propeller for VTOL.

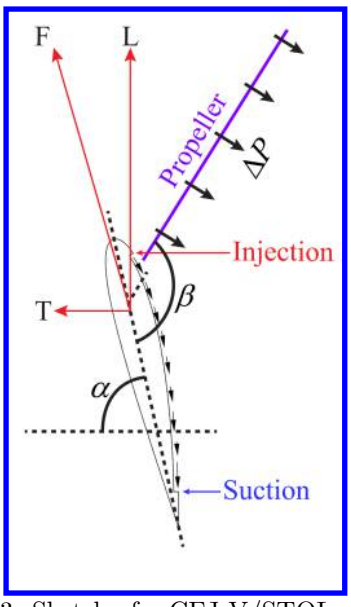

Figure 3: Sketch of a CFJ-V/STOL concept.

The CFJ-VTOL concept was suggested by Zha et al in 2019.[16] It is to utilize the advanced CFJ airfoil

with propellers to generate substantial hovering lift from the CFJ wings instead of from the propellers only. The CFJ airfoil can sustain very high angle of attack[14,15] with ultra-high lift coefficient and is virtually stall free. However, at static hovering condition, the CFJ airfoil itself will not generate high lift unless there is freestream flowing toward the airfoil.

The CFJ-VTOL concept[16] is depicted in Fig. 2 and 3, which has propellers mounted on the upper surface of a CFJ wing. The propeller does not completely face upward as conventional VTOL aircraft that rely on the propellers to generate all the lift. The propeller of CFJ-VTOL faces upward and forward as shown in Fig. 3. It generates a partial lift for the VTOL system and induces freestream to the CFJ airfoil at static hovering condition. Enhanced by the freestream, the CFJ airfoil at a very high angle of attack(e.g. 80°) will generate a ultra-high lift coefficient at a much lower power consumption than the propellers.

Figure 4: High speed CFJ VTOL from takeoff to cruise

Fig. 4 shows the proposed CFJ-VTOL vehicle, which uses a tandem wing configuration with no vertical tail. The advantages of tandem wing configuration include: 1) generating lift from two lifting vectors for hovering with high stability; 2) high structure strength and high aircraft maneuverability; 3) overcoming the increased pitching moment coefficient of CFJ wings caused by high lift; 4) more compact size. But the tandem wings may suffer some aerodynamic efficiency loss due to reduced aspect ratio and wing-wing interference.

Fig. 4 on the left shows the vehicle at hovering mode with the wing tilted to 80°. At cruise, the wing is tilted to horizontal as shown on the right in Fig. 4. The tailless flight control concept is to use different coflow jet and propeller strength along the span to create unbalanced lift and thrust (or drag) to generate the rolling moment, yaw moment, and pitching moment with the tandem wings. The CFJ and propeller strengths will be controlled at different span locations by the micro-compressor power and propeller motor power, e.g. RPM.

The wing planform area is sized to cruise at Mach 0.6 at the altitude of 41,000 ft with a payload of 1500 kg. The aspect ratio of the tandem wing system is 18.7 considering the fuselage width as a part of the wing span. The maximum wing span is 13.57 m and the total wing area is 12 m^2. A series of propellers are installed downstream of the CFJ injection (see Fig. 2 and 3) to form a distributed propulsors with the CFJ micro-compressors embedded inside the wing. The diameter of the propellers is equal to the wing chord to enable the high speed cruise with low tip speed to have high efficiency. This makes the propeller actuator disk size area the same as the wing area.

II. Methodology

II.A. CFJ Airfoil Parameters

II.A.1. Drag and Lift

Zha et al.[4] give the following formulations to calculate the lift and drag due to CFJ effect for CFD simulation

$$R_x = (\dot{m}_j V_{j1} + p_{j1} A_{j1})\ cos(\theta_1 - \alpha) - (\dot{m}_j V_{j2} + p_{j2} A_{j2})\ cos(\theta_2 + \alpha) \tag{3}$$

$$R_y = (\dot{m}_{j1} V_{j1} + p_{j1} A_{j1})\ sin(\theta_1 - \alpha) + (\dot{m}_{j2} V_{j2} + p_{j2} A_{j2})\ sin(\theta_2 + \alpha) \tag{4}$$

where x and y represent the drag and lift direction respectively, subscripts 1 and 2 stand for the injection and suction, θ_i $(i = 1, 2)$ is the angle between the injection or suction slot surface and the line normal to the airfoil chord, and α is the AoA, as shown in Figure 5.

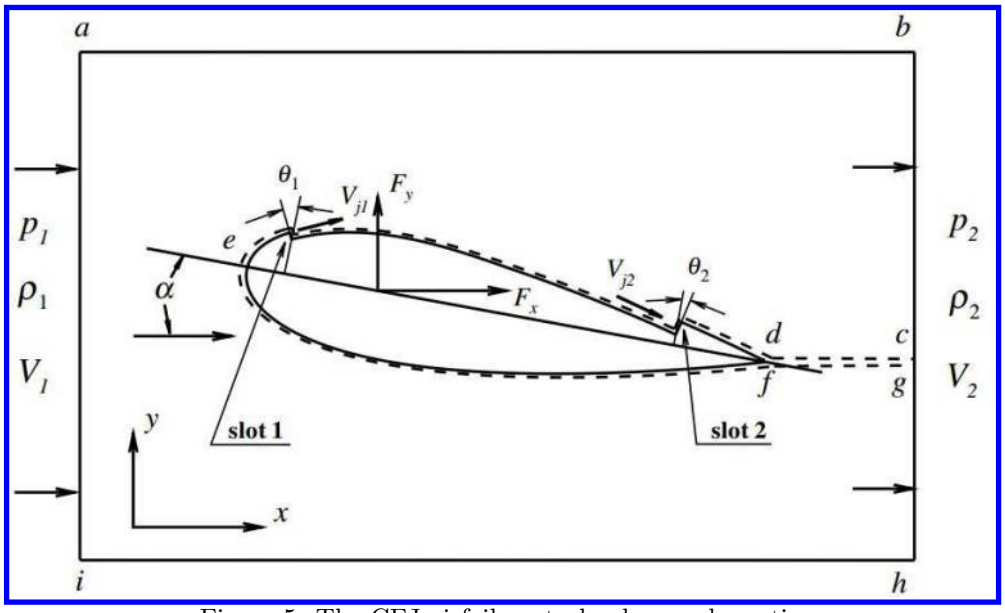

Figure 5: The CFJ airfoil control volume schematic.

The total drag and lift of the CFJ airfoil can then be expressed as below

$$D = F_x - R_x \tag{5}$$

$$L = F_y - R_y \tag{6}$$

where F_x and F_y are the drag and lift force due to surface integral of pressure and shear stress. The corresponding drag and lift coefficients are expressed as following

$$C_D = \frac{D}{\frac{1}{2}\rho_\infty {V_\infty}^2 S} \tag{7}$$

$$C_L = \frac{L}{\frac{1}{2}\rho_\infty {V_\infty}^2 S} \tag{8}$$

where ρ_∞ and V_∞ denote the free stream density and velocity. S is the wing planform area. For 2-D airfoil study, S denotes the planform area per unit span, which is equal to the airfoil chord length.
The maximum lift coefficient for potential flow is imposed by the Kutta-condition which does not reflect physical limits when adding energy to the flow via active flow control.

$$C_{Lmax} = 2\pi(1 + t/c) \tag{9}$$

With active flow control, there seems to be no law written for maximum lift coefficient, and anything breaking traditional limits is known as "Super-Lift".

II.A.2. Jet Momentum

The jet momentum coefficient C_μ is a parameter used to quantify the jet intensity, which is defined as

$$C_\mu = \frac{\dot{m} V_j}{\frac{1}{2}\rho_\infty {V_\infty}^2 S} \tag{10}$$

where $\dot{m}$ is the injection mass flow rate, V_j is the averaged injection velocity at the injection slot opening.

II.A.3. Power Consumption

The CFJ can be implemented by mounting a pumping system inside the wing that withdraws air from the suction slot and blows it into the injection slot. The power consumption can be determined by the jet mass flow and total enthalpy change as follows

$$P = \dot{m}(H_{01} - H_{02}) \tag{11}$$

where H_{01} and H_{02} are the total enthalpy in the injection cavity and suction cavity, respectively. P is the power required by the pump. Introducing the pump efficiency η and total pressure ratio of the pump $\Gamma = \frac{P_{01}}{P_{02}}$, the power consumption can be expressed as

$$P = \frac{\dot{m} C_p T_{02}}{\eta} (\Gamma^{\frac{\gamma-1}{\gamma}} - 1) \tag{12}$$

where γ is the specific heat ratio for air. The power consumption can be further normalized as a power coefficient

$$P_c = \frac{P}{\frac{1}{2}\rho_\infty V_\infty^3 S} \tag{13}$$

II.A.4. Aerodynamic Efficiency

The conventional airfoil aerodynamic efficiency is defined as

$$(\frac{L}{D}) = \frac{C_L}{C_D} \tag{14}$$

For the CFJ airfoil, the ratio above represents the pure aerodynamic relationship between lift and drag. Taking into account the energy consumption of the CFJ, the conventional aerodynamic efficiency is modified by converting the power consumption into a corresponding drag force. The equation of the corrected aerodynamic efficiency is given as follows[9]

$$(\frac{L}{D})_c = \frac{L}{D + \frac{P}{V_\infty}} \tag{15}$$

in which the pump power consumption P is converted into a force $\frac{P}{V_\infty}$ added to the aerodynamic drag D. The formulation above can be further expressed using the non-dimensional coefficients C_L, C_D and P_c as

$$(\frac{L}{D})_c = \frac{C_L}{C_D + P_c} \tag{16}$$

Note that when the pumping power is set to 0, $(\frac{L}{D})_c$ returns to conventional aerodynamic efficiency definition.

A new parameter, the productivity coefficient was introduced by Yang et al.[14] It describes the the capability to transport a gross weight for maximum distance at cruise.

$$(\frac{C_L^2}{C_D})_c = \frac{C_L^2}{C_D + P_c} \tag{17}$$

This study involves a tandem wing configuration. For example, the coefficient of lift for each wing can be defined individually as:

$$C_{L1} = \frac{L_1}{\frac{1}{2}\rho_\infty {V_\infty}^2 S_1}, \quad C_{L2} = \frac{L_2}{\frac{1}{2}\rho_\infty {V_\infty}^2 S_2}, \tag{18}$$

where the subscript 1 and 2 stand for the first and second wing. For the aircraft system with tandem wings, the system lift coefficient is defined as the total lift based on the total wing area below:

$$C_{Lt} = \frac{L_1 + L_2}{\frac{1}{2}\rho_\infty {V_\infty}^2 (S_1 + S_2)} \tag{19}$$

where the subscript t stands for tandem wing.

Substituting Eq. (18)to Eq. (19), the system lift coefficient can be expressed as:

$$C_{Lt} = \frac{C_{L1} S_1 + C_{L2} S_2}{S_1 + S_2} \tag{20}$$

Eq. (20) is actually the same as the area weighted lift coefficient. Similarly, the coefficient of system drag and CFJ power can be defined as:

$$C_{Dt} = \frac{C_{D1}S_1 + C_{D2}S_2}{S_1 + S_2} \tag{21}$$

$$P_{ct} = \frac{P_{c1}S_1 + P_{c2}S_2}{S_1 + S_2} \tag{22}$$

The corrected drag coefficient is:

$$(C_{Dc})_t = C_{Dt} + P_{ct} \tag{23}$$

The aerodynamic efficiency and the productivity efficiency of the tandem wing system then can be defined following the same way as Eq. (16) and Eq. (17). To see the relations clearly, we take the aerodynamic efficiency of the tandem wing as an example below:

$$\begin{aligned}(\frac{L}{D_c})_t &= \frac{L_1 + L_2}{D_1 + D_2 + P_1/V_\infty + P_2/V_\infty} = \frac{C_{Lt}\frac{1}{2}\rho_\infty {V_\infty}^2(S_1 + S_2)}{C_{Dt}\frac{1}{2}\rho_\infty {V_\infty}^2(S_1 + S_2) + P_{ct}\frac{1}{2}\rho_\infty {V_\infty}^2(S_1 + S_2)} \\ &= \frac{S_1C_{L1} + S_2C_{L2}}{S_1C_{D1} + S_2C_{D2} + S_1P_{c1} + S_2P_{c2}}\end{aligned} \tag{24}$$

That is:

$$(\frac{L}{D_c})_t = \frac{C_{Lt}}{(C_{Dc})_t} \tag{25}$$

Propeller disk loading (D_L) and power loading (P_L) are used to describe the performance of VTOL hovering and are defined as:

$$D_L = L/A, \quad P_L = P/L \tag{26}$$

where L is the lift generated by the propeller, A is the propeller disk area, P is the propeller required power to generate the lift, L. Power loading describes the power required per unit lift.

The disk loading coefficient is:

$$D_{L_c} = \frac{L/(1/2\rho V^2 S)}{A/S} = \frac{C_L}{A_c} = \frac{D_L}{\frac{1}{2}\rho V_\infty^2} \tag{27}$$

Where $A_c = A/S$, and A is the disk area and S is the wing planform area. The power loading coefficient is:

$$P_{L_c} = \frac{P/(1/2\rho V^3 S)}{L/(1/2\rho V^2 S} = \frac{P_p}{C_L} = \frac{P_L}{V_\infty} \tag{28}$$

The power coefficient for the propeller actuator is:

$$P_P = \frac{2}{\rho V_\infty^3 S}\sqrt{\frac{F^3}{2\rho A}} \tag{29}$$

where F is the total force produced by the propeller actuator normal to the propeller disk.

During hovering, the following relations apply based on 1D actuator disk theory:

$$P_L = \sqrt{D_L \frac{1}{2\rho}} \tag{30}$$

$$P_{L_c} = \frac{\sqrt{D_{L_c}}}{2} \tag{31}$$

For a CFJ-VTOL system, the lift will be generated by both the propeller and the wing. Thus the power loading can be used for the whole system or for each component such as the propeller or the wing.
For the system,

$$P_{L_{CFJ-VTOL}} = \frac{P_{CFJ} + P_{actuator}}{L_{CFJ} + L_{actuator}} \tag{32}$$

For the component,

$$P_{L_{CFJ}} = \frac{P_{CFJ}}{L_{CFJ}} \tag{33}$$

$$P_{L_{actuator}} = \frac{P_{actuator}}{L_{actuator}} \tag{34}$$

II.B. Numerical Approach

The in house FASIP (Flow-Acoustics-Structure Interaction Package) CFD code is used to conduct the numerical simulation. A 3rd order WENO scheme for the inviscid flux and a 2nd order central differencing for the viscous terms are employed to discretize the Navier-Stokes equations. The low diffusion E-CUSP scheme used as the approximate Riemann solver suggested by Zha et al[17] is utilized with the WENO scheme to evaluate the inviscid fluxes. Implicit time marching method using Gauss-Seidel line relaxation is used to achieve a fast convergence rate. Parallel computing is implemented to save wall clock simulation time.[18]

II.C. Boundary Conditions

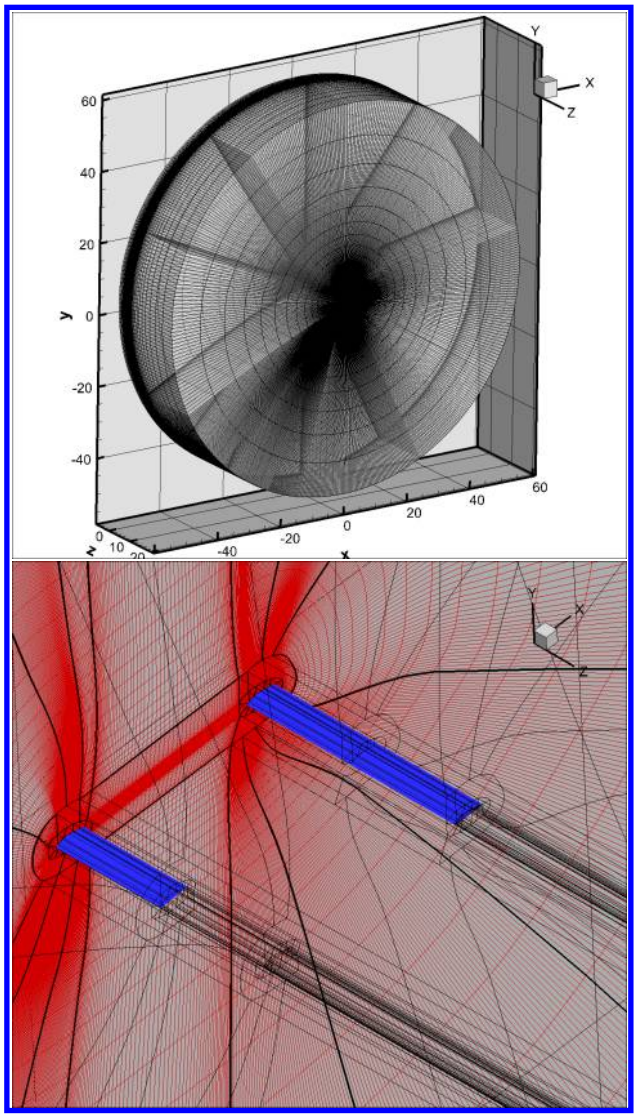

Figure 6: CFD Domain

For the 3D tandem wing cruise simulation, the mesh topology and domain near the wings are shown in Figure 6. The computational domain has O-mesh topology and the radial far-field boundary is located 55 chord lengths. The spanwise far-field is located 20 chord away from the wing tip. Total pressure, total temperature and flow angles are specified at the injection duct inlet, as well as the upstream portion of the far field. Constant static pressure is applied at the suction duct outlet as well as the downstream portion of the far field. Symmetry boundary conditions are applied at the root of the wing, whereas the wing top flow is resolved by a mesh block. The cross-section faces of the CFJ ducts are meshed using "H" topology while the domains around the airfoil are meshed using "O" topology The total mesh size is 10.4 million cells, split into 193 blocks for parallel computation. The first grid point on the wing surface is placed at y+ = 1. The actuator disk BC is modeled as a flat surface, across which the static pressure is increased by a percentage ΔP based on the local static pressure upstream of the disk. Even though the pressure increase percentage is uniform across the disk, the pressure increase is not due to the non-uniform local static pressure upstream of the disk. Each Tandem Wing was run at Mach 0.6 and $Re = 5.35 \times 10^6$. The aspect ratio of the wing is 11.65. The CFJ wing suction surface between the injection slot and suction slot is translated downward 0.6% chord. The injection slot size is 1.2%C and the suction slot size is 2.45%C.

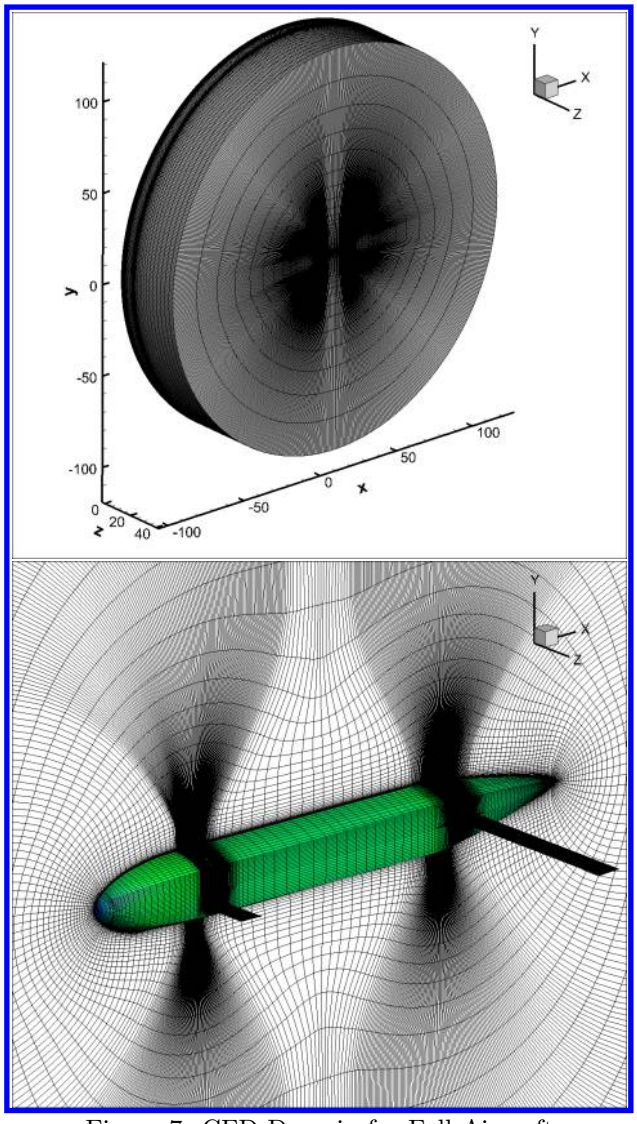

Figure 7: CFD Domain for Full Aircraft

Similarly, the full aircraft is also modeled including the fuselage. The domain can be seen in Figure 7. This is also based on an O-mesh topology. The radial far-field is located at 120 chord lengths, with the spanwise far-field located 40 chord lengths from the fuselage center-line. The total mesh size is 11.5 million cells split into 226 blocks. The boundary conditions for the wings and CFJ ducts are identical to the

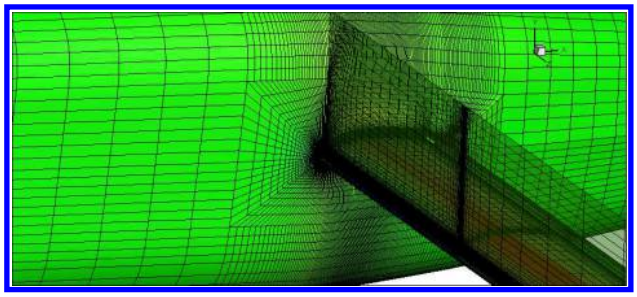

Figure 8: Wing and actuator meeting fuselage

tandem wing mesh. The flow conditions are also the same. Figure 8 shows the surface grid of the rear wing meeting the surface grid of the fuselage. There is an O-mesh topology around the wing for good quality. This blends into the fuselage H-mesh. The actuator block boundary is seen as the translucent block above the wing. The CFJ injection and suction slots are inside the wing. The mesh is clustered near the wingtip. This clustering is carried downstream to resolve the wingtip vortex. This is seen mid-span on the rear wing in Figure 8.

III. Results and Discussions

III.A. Initial Configuration for Cruise Efficiency

The initial results from the previous tandem wing study,[19] which focuses mainly on cruise efficiency, is analyzed for longitudinal static stability. The front wing has an aspect ratio of 14, while the rear wing has an aspect ratio of 7. This puts the front wing with the large, more effective lifting surface out of the way of any negative downwash effects. Similarly, this removes the rear wing from being in the trajectory of the wing tip vortex of the lead wing. The wings are spaced 8 chord lengths axially, and 1.5 chord lengths vertically. These values are chosen to fit on a fuselage with a mission of 15 passenger or 1.5 ton payload. The CFJ jet is maintained at C_μ of 0.01 at level flight. As a more effective control law observed by Wang and Zha,[20] the injection total pressure corresponding to the optimum C_μ at cruise condition is fixed for the angle of attack variation of the pitching momentum study.

The computed pitching moment coefficient (C_M), lift coefficient, and corrected aerodynamic efficiency for this tandem wing configuration with no fuselage are given in Figure 9. Figure 9 shows that the pitching moment is trimmed at cruise condition at AoA of 0° and the optimal $(C_L/C_D)_c$, but the slope is positive and is not statically stable.

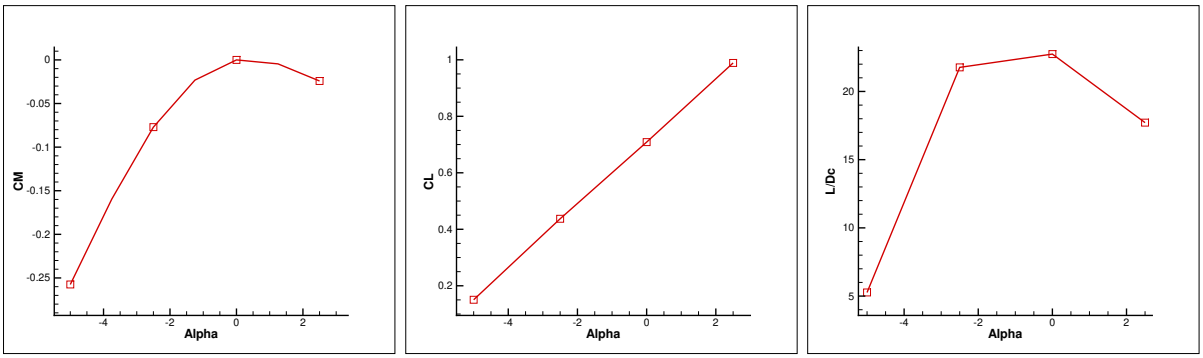

Figure 9: Wing 1 AR14, Wing 2 AR7

III.B. Fuselage

The fuselage used for the full aircraft simulation from the previous study[19] is not optimized for several reasons. The drag of the fuselage is high because 1) the fuselage is too wide for the mission with the volume more than required; 2) the wing fuselage junction is not treated well and it increases drag due to flow separation; 3) the fuselage creates large nose down pitching moment at negative angle of attack.

The purpose of this section is to redesign a fuselage to overcome the drawbacks mentioned above.

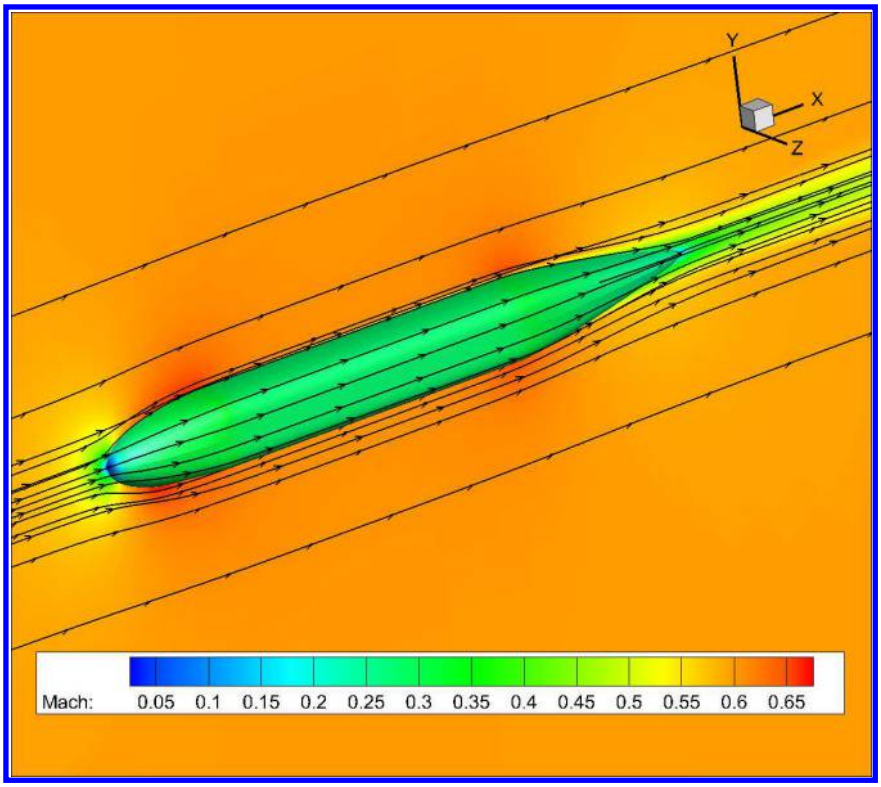

Figure 10: New Aircraft Fuselage, $C_D = 0.018$

Figure 10 shows the results of redesigned fuselage. The sides are flatter where the wings meet the fuselage. This will provide less flow interaction on the wings. The drag coefficient of the fuselage is only 0.018. The fuselage diameter is 2m, and it is 17m long to keep the same mission requirement of 15 seats or 1.5 ton payload. The chord length of the wings is 0.756m. The overall reference area of the wings is 10.5m to cruise at 41,000 ft altitude at Mach number 0.6.

III.C. Tandem Wing Aspect Ratio Study

To understand the tandem wing effect on pitching moment with no fuselage, a trade study is done for the aspect ratio distribution between the front and rear wing while keeping the same total wing area and the chord unchanged. The purpose is to search the aspect ratio for optimal cruise efficiency and longitudinal stability. Table 1 lists all the cases studied at AoA of $-5°$. Case 1 and 2 have the front wing aspect ratio twice larger than the rear wing. They generate large nose down pitching moment when the AoA is $-5°$. Various aspect ratio is studied with the front wing size 3 times larger than the rear wing, 2 times larger, equal, 1/3, 1/4. The required nose up pitching moment is obtained when the front wing size is 1/3 and 1/4 of the rear wing. A few representative cases are described below to provide some more detailed information.

III.C.1. Case 8: Wing 1 AR7, Wing 2 AR14

Putting the larger, primary lifting wing in the rear is shown to negatively affect the tandem wing system aerodynamic efficiency due to downwash and wake interaction from the front wing. However, canard-wing configurations usually have the smaller aspect ratio canard in front of the center of gravity for the aircraft. We then also observe that using the smaller aspect ratio wing in the front and the larger aspect ratio wing in the rear is beneficial to the longitudinal stability. The pitching moment coefficient when the system is at a an angle of attack of $-5°$ is improved, compared with when the larger wing is in front.

In Figure 11, the smaller wing with AR 7 is in the front and the twice larger wing is in the rear. The propeller actuator disk can be seen as the translucent plane above the suction surface of both wings. This has a negative impact on longitudinal stability, as it produces a nose-down pitching moment. The

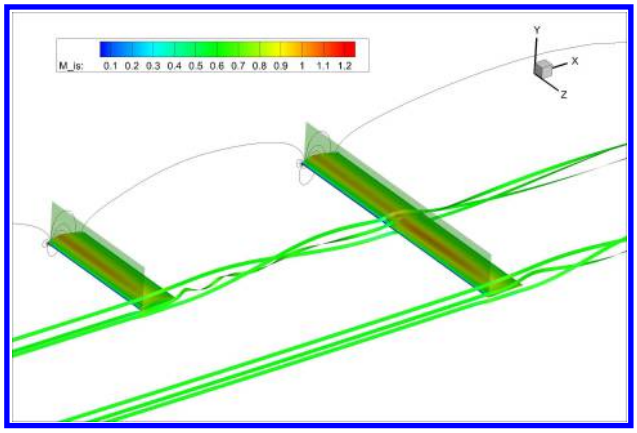

Figure 11: Case 8, Wing 1 AR7, Wing 2 AR14, $i_1 = 2°$, $i_2 = 0°$

propeller effect on pitching moment effect is not very strong, but needs to be taken into account when determining the aerodynamic center and pitching moment coefficient. When the aerodynamic center at cruise is determined with $\alpha = 0°$, the pitching moment coefficient of the aircraft system is calculated for the angle of attack of $-5°$. Results are given in Table 1.

Table 1: Pitching moment coefficient at $\alpha = -5°$ for various front and rear wing aspect ratio and incidence angles

Case	AR_1/AR_2	$i_1(°)$	$i_2(°)$	**CM**
1	2	0.5	0	-0.6013
2	2	1.5	0	-0.2295
3	3	0.5	0	-0.2640
4	3	0.5	-1	-0.2060
5	1	0.5	0	-0.1603
6	1	0.5	-2	-0.0303
7	0.5	0	0	-0.1229
8	0.5	2	0	-0.0186
9	0.333	0	0	-0.0700
10	0.333	1	0	-0.0420
11	0.333	3	0	0.0788
12	0.25	0	0	-0.0564
13	0.25	1	0	-0.0437
14	0.25	2	0	0.0136
15	0.25	3	0	0.0731

Starting with our initial configuration with AR 7 in the front and AR14 in the rear, increasing the loading on the front wing by increasing its incidence angle improves the pitching moment coefficient. Ultimately, the pitching moment should be positive at lower angles of attack when the lift coefficient is zero. A similar effect is seen by reducing the incidence angle of the rear wing. Throughout this study, high aerodynamic efficiency is kept as a constraint, so reducing the angle of attack on the larger wing will hurt our overall lift coefficient and is not the most desirable.

III.C.2. Case 9-11: Wing 1 AR 5.25, Wing 2 AR 15.75

Decreasing the front wing to be only 1/3 the span of the rear wing substantially reduces the nose-down pitching moment to -0.07 at $\alpha = -5°$. As we have learned, increasing the loading of the front wing is helpful. This case maintains the same axial and vertical spacing as the other cases, 8 chord lengths axially and 1 chord length vertically, as well as the same injection slot total pressure corresponding to C_μ of 0.01 at level flight. Figure 12 shows the Mach number contours with streamlines for the Case 9.

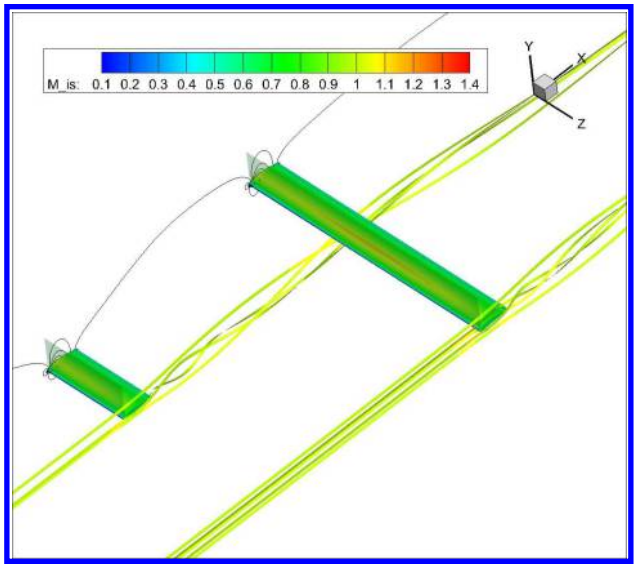

Figure 12: Wing 1 AR 5.25, Wing 2 AR 15.75

Increasing the loading of the front wing in this configuration by increasing the incidence angle from 0° to 1° (Case 10) shows a benefit in Table 1. The pitching moment coefficient is changed from -.07 to -.04. As shown in Figures 13 and 14 for the isentropic Mach number distribution along the span at 0° and 1° incidence angles, the loading clearly increased.

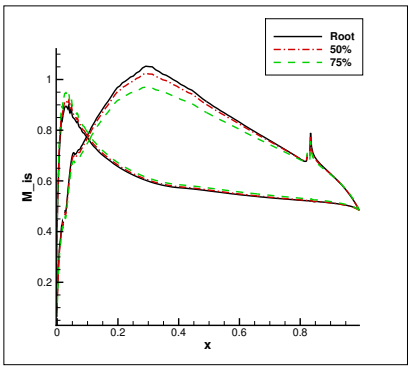

Figure 13: Isentropic Mach Distributionof Front Wing at $i = 0°$

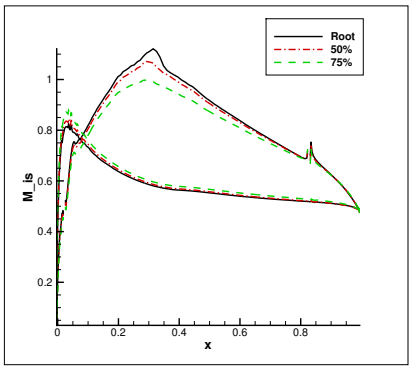

Figure 14: Isentropic Mach Distribution of Front Wing at $i = 1°$

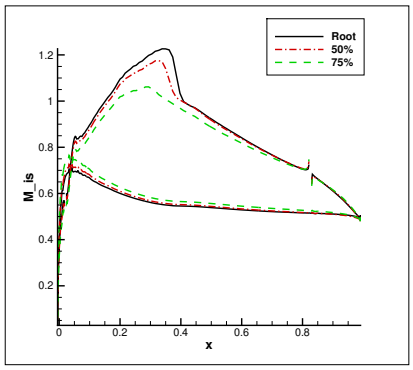

Figure 15: Isentropic Mach Distribution of Front Wing at $i = 3°$

Increasing the front wing incidence angle to 3° provides even better pitching moment. The pitching moment coefficient at $\alpha = -5°$ is 0.0788, a nose-up moment. The wing-loading at cruise is higher as well. The corrected aerodynamic efficiency at $\alpha = 0°$ is 21.6. This is a reduction from the peak efficiency near L/D_c of 24 for Case 1. This indicates the conflict between the cruise efficiency and pitching stability.

III.C.3. Case 12-15: Wing 1 AR 4.2, Wing 2 AR 16.8

The best pitching moment results when the front wing size and aspect ratio are one quarter of the rear wing. This also makes the rear wing aspect ratio increased, which means a longer span and more efficient wing.

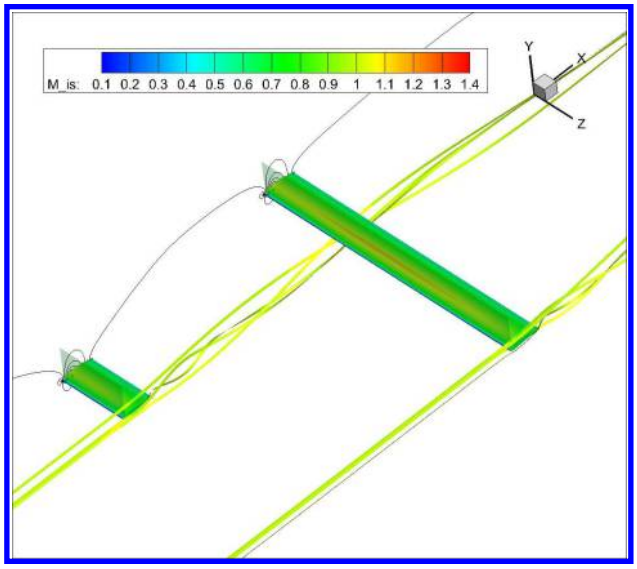

Figure 16: Wing 1 AR 4.2, Wing 2 AR 16.8

Increasing the incidence angle of the front wing from 2° (Case 14) to 3° (Case 15) increases the nose up pitching moment when the system angle of attack is at $\alpha = -5°$. The Case 15 configuration also achieves a high aerodynamic efficiency shown in Table 2. The corrected aerodynamic efficiency is 23.16 is only slightly lower than the peak aerodynamic efficiency configuration from the previous study, which has the front wing aspect ratio to rear wing aspect ratio of $2:1$. The Isentropic Mach distribution of the front and rear wings can be seen in Figure 17. The high incidence angle of the front wing overcomes the low aspect ratio and provides relatively high lift. There is a shock wave but it is not strong enough to be a detriment to performance. The inner rear wing span suffers from a lower effective angle of attack, while the outer span performs quite well. Overall, this allows for a $(C_L/C_D)_c$ of 23.16 at cruise.

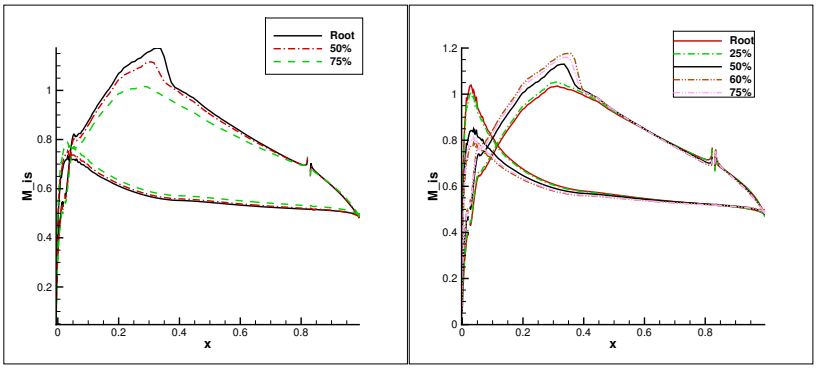

Figure 17: Case 15 Isentropic Mach number distribution; (A)Wing 1 AR 4.2 $i_1 = 3°$, (B)Wing 2 AR 16.8 $i_2 = 0°$

Table 2: AR1/AR2 = 0.25, $i_1 = 3°$, $i_2 = 0°$

	CL	**CD**	**Pc**	**CL/CD**	**CL/CDc**	**CLˆ2/CDc**
Wing 1	0.7646	0.0496	0.0056	15.4143	13.8508	10.5899
Wing 2	0.7450	0.0201	0.0065	37.0447	27.9916	20.8529
Overall	0.7489	0.0260	0.0063	28.7943	23.1630	17.3465

The reason placing the low aspect ratio wing in the front is beneficial for pitching stability is that the lower aspect ratio of a 3D wing will have a lower slope of the lift coefficient vs AoA. In other words, the front wing will have lower sensitivity about AoA than that of rear wing that has a much higher aspect ratio.

III.D. Full Aircraft

The full aircraft simulation uses the same mesh described in Section 10.2.1. The front wing aspect ratio is 4.2, and the rear wing aspect ratio is 16.8 The wings are separated vertically by 1 chord length, as they are in the tandem wing study. The wings are separated longitudinally by 13 chord lengths. This is more than the 8 chord lengths in the static stability study. The extra distance increases the moment arm for the wings to help with nose-up pitching moment. The full aircraft Mach number contours with streamlines are shown in Figure 18.

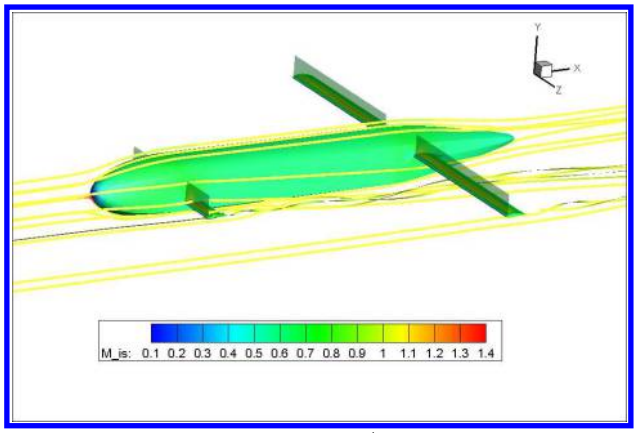

Figure 18: Fuselage with wings. AR1/AR2 = 0.25, $i_1 = 3°$, $i_2 = 0°$

Fig. 19 displays the mid-span isentropic Mach number distribution of the front wing with the fuselage. The result is very similar to the one given in Fig. 17 with no fuselage. It indicates that the fuselage interaction with the front wing is minimized.

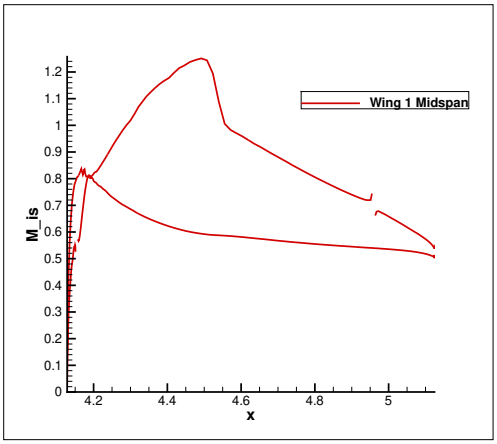

Figure 19: Wing 1 AR 4.2 $i_1 = 3°$ Isentropic Mach distribution

The goal in redesigning the fuselage is to decrease the pitching momentum contribution of the fuselage and reduce drag. Overall at cruise, the aircraft system has a higher aerodynamic efficiency than that designed in the previous study.[19] The overall drag value is reduced slightly, and the lift is increased. The wing performance has a $(C_L/C_D)_c$ of 22.2, which is only a 4.2% reduction compared with the simulation without the fuselage. Lift and drag of the wings were both slightly increased. The aircraft aerodynamic efficiency increased by 2.3% compared to the results from the previous study.

Table 3: Aerodynamic performance of the redesigned VTOL vehicle at cruise; AR1/AR2 = 0.25, $i_1 = 3°$, $i_2 = 0°$

	C_L	C_D	C_M	P_c	C_L/C_D	C_L/C_{D_c}	C_L^2/C_{D_c}
Wing 1	0.7576	0.0518	1.3861	0.0057	14.6148	13.1566	9.9678
Wing 2	0.7513	0.0216	-1.6442	0.0064	34.8483	26.8668	20.1858
Wings 1+2	0.7526	0.0276	-0.2581	0.0063	27.2484	22.2051	16.7117
Fuselage	0.0680	0.0210	0.2581	0.0000	-	-	-
Overall	0.8206	0.0486	0.0000	0.0063	16.8779	14.9489	12.2671

At lower angles of attack, the pitching moment coefficient goes negative. This is due to the pitching moment contribution of the fuselage itself. In order to counteract the effect of the fuselage on pitching moment at low angle of attack, the fuselage is given a positive incidence angle. Reducing the angle of attack by an amount equal to the fuselage incidence angle should counteract most of the fuselage contribution to pitching moment at low angle of attack and allow the tandem wing configuration to provide a positive pitching moment.

III.D.1. Fuselage Incidence Angle Study, $i = 5°$

The increase in fuselage incidence angle is initially tried at $i_f = 2°$. The pitching moment coefficient at an AoA of $-5°$ is still negative resulting in nose-down force generation. Increasing the incidence angle to $i_f = 5°$ provides more favorable results. Figure 20 shows Mach contours around the fuselage center line, with the fuselage incidence angle of 5° at cruise. The entire aircraft at 0° angle of attack cruise conditions is shown in Figure 21. The front and rear wings are still spaced 13 chord lengths. The center of gravity, where the trimmed pitching moment at cruise is located at 53% of the fuselage length.

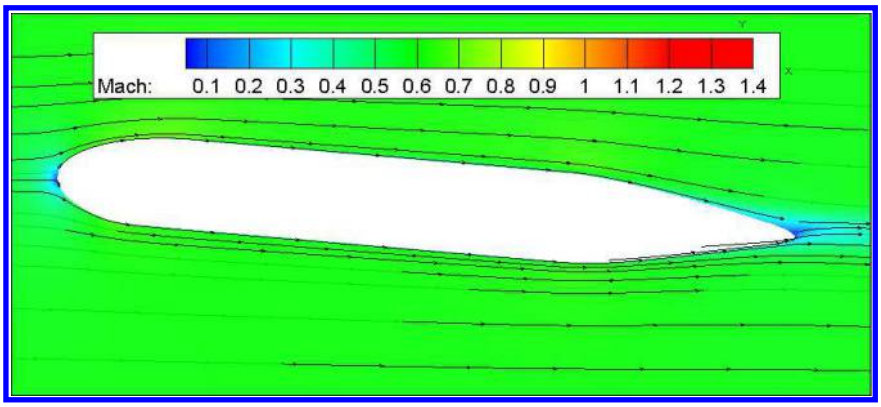

Figure 20: Fuselage incidence angle, $i = 5°$

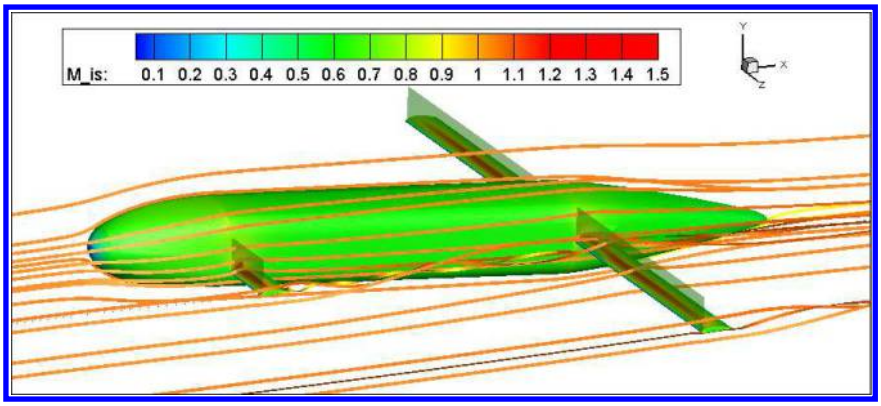

Figure 21: Full Aircraft at cruise, AoA = 0, Fuselage incidence angle, $i_f = 5°$, $i_1 = 3°$, $i_2 = 0°$

Figure 22 shows Mach contours slices along the span of the front wing (left) and rear wing (right), normalized by the wing chord. The origin location is the root of the wings. It is clear that the front wing is at a higher incidence angle, $i_1 = 3°$. The smaller aspect ratio and higher incidence results in higher wing loading. The loading is reduced toward the tip. The incidence of the rear wing is 0°. The inner span of the rear wing is directly affected by the front wing's downwash, which makes the inner part of the rear wing less loaded than the outerspan as shown in Fig. 22.

Figure 23 shows span-wise slices of the front and rear wings when the aircraft angle of attack is 2°. The front wing has a flow separation near the the root of the wing. The separation limits the maximum C_μ value of the front wing.

Table 4 lists the aerodynamic performance decomposition of the wings, fuselage, and overall aircraft at cruise with system AoA of 0°. Since the fuselage incidence angle is higher, it contributes a lift coefficient of 0.17. The overall vehicle lift coefficient is 1. The cruise efficiency is still very high at 15.33 with cruise Mach number of 0.6. Since the front wing has a small aspect ratio at high incidence angle, the drag coefficient is higher than the rear wing. This does not have a large effect on the overall system drag as the high aspect ratio rear wing is weighted more significantly in the overall lift and drag calculations.

At cruise with angle of attack zero, the nose-up pitching moment contribution of the front wing is smaller in magnitude than the nose-down pitching moment contribution of the rear wing. At lower angles of attack, the low incidence angle of the rear wing will have less effect on pitching moment contribution than the front wing. This is represented in Figure 24, in which the C_M, C_L and C_D values at different angles of attack are plotted for the wings, fuselage and overall system. It can be seen that the overall pitching moment slope is negative, except when the AoA is smaller than $-5°$. The negative pitching moment slope is mostly contributed by the rear wing, which is caused by the higher slope of the rear wing due to higher aspect ratio. These results indicate that a tandem wing configuration for VTOL can be indeed designed to have sufficient static stability margin with high cruise efficiency. Difficulties for the static stability occurs when the AoA is above $\alpha = 2°$ due to separation near the root of the wings preventing the sufficient mass flow rate for CFJ. Insufficient static stability also occurs when the AoA is less than -8deg.

Table 4: New Fuselage With Wings: AR1/AR2 = 0.25, $i_f = 5$, $i_1 = 3°$, $i_2 = 0°$, $\alpha = 0°$

	C_L	C_D	P_c	C_M	C_L/C_{Dc}	C_L^2/C_{Dc}	AR
Wing 1	0.9149	0.0463	0.0168	1.3950	14.5016	13.2670	4.2
Wing 2	0.8148	0.0167	0.0070	-2.3111	34.4151	28.0407	16.8
Wings 1+2	0.8348	0.0226	0.0089	-0.9162	26.4532	22.0831	14.28
Fuselage	0.1701	0.0340	-	0.9162	-	-	-
Overall	1.0049	0.0566	0.0089	0.0000	15.3359	15.4106	14.28

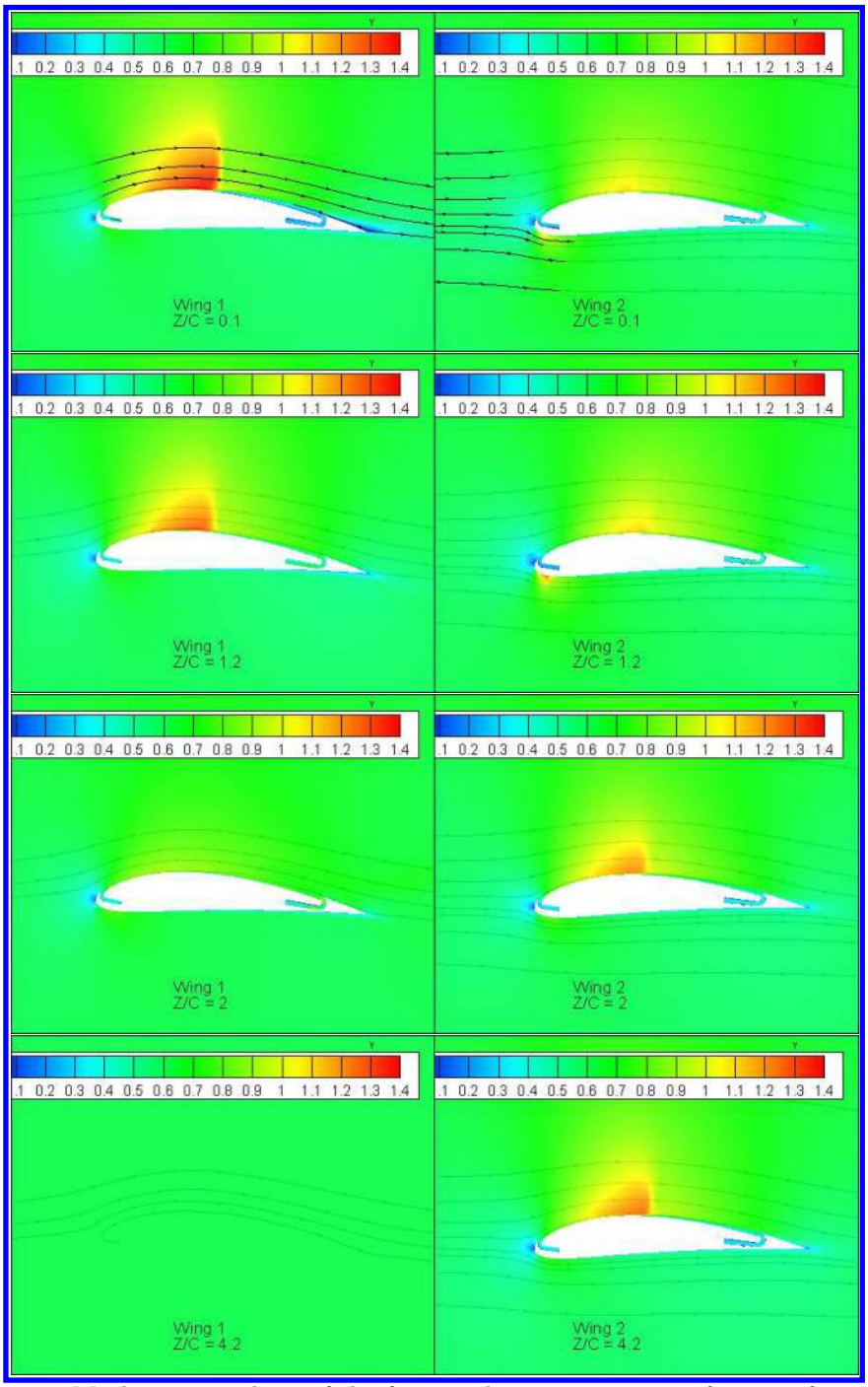

Figure 22: Mach contour slices of the front and rear wings, $\alpha = 0°$, $i_f = 5°$, $i_1 = 3°$, $i_2 = 0°$

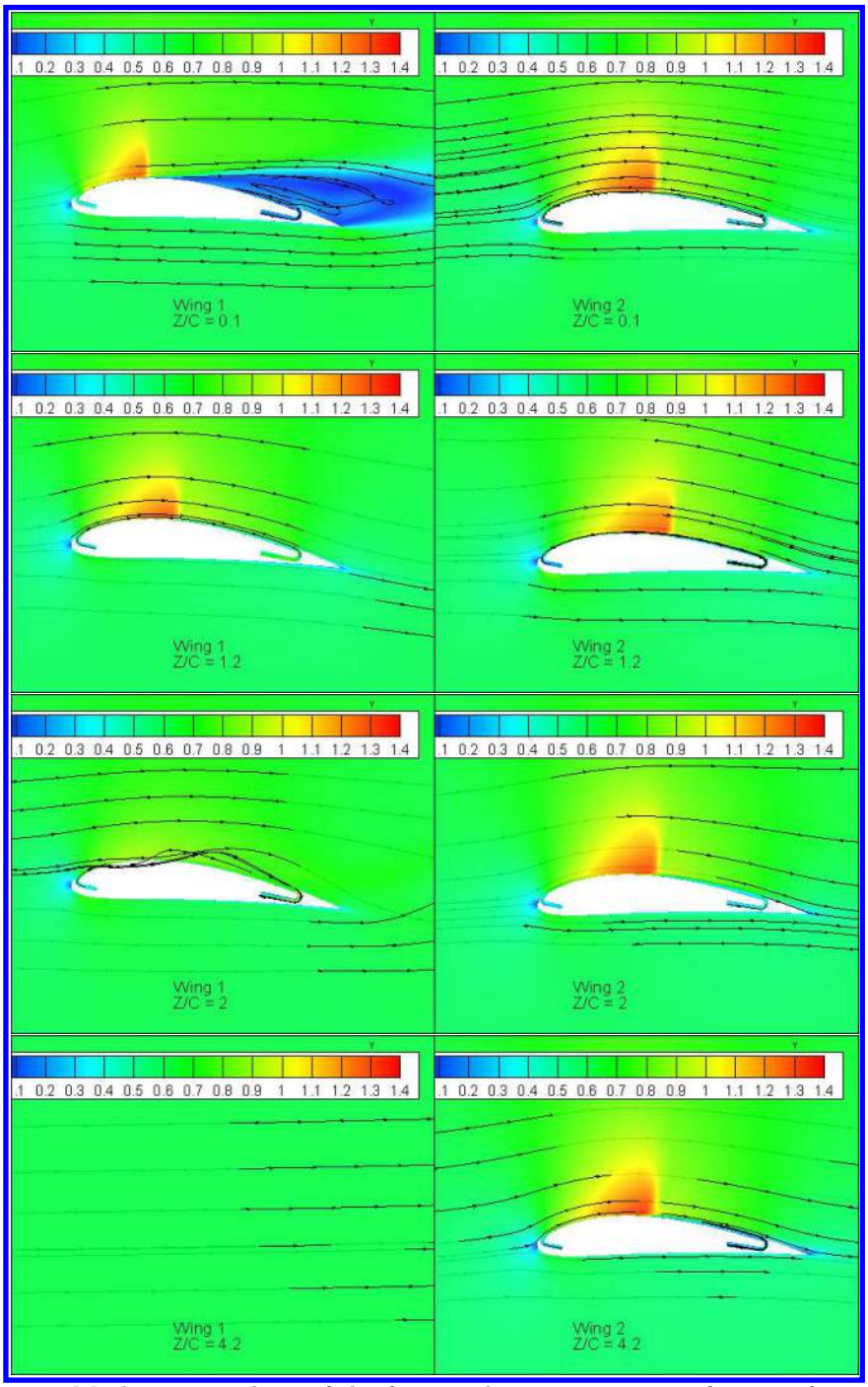

Figure 23: Mach contour slices of the front and rear wings, $\alpha = 2°$, $i_f = 5°$, $i_1 = 3°$, $i_2 = 0°$

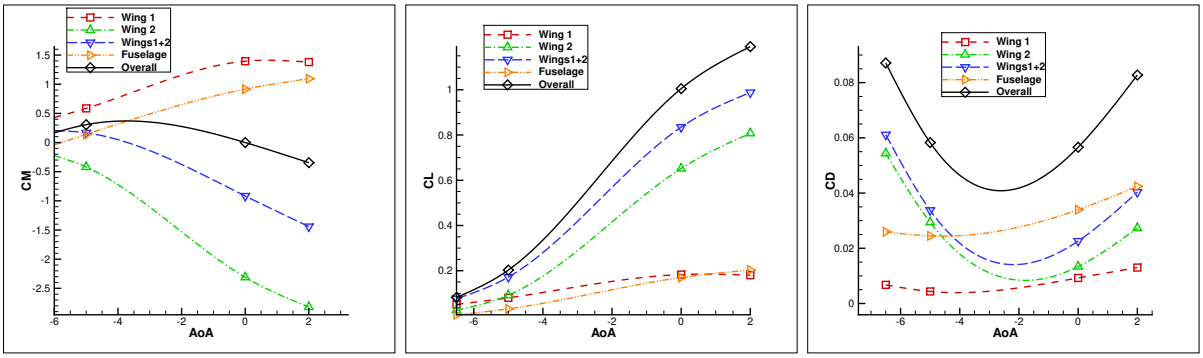

Figure 24: C_M, C_L, and C_D vs AoA, $i_f = 5°$, $i_1 = 3°$, $i_2 = 0°$

IV. Conclusions

The study in this paper indicates that a high speed VTOL vehicle using tandem wing at cruise Mach number 0.6 can achieve very high aerodynamic efficiency of 15.3 while having sufficient longitudinal static stability. To achieve the longitudinal stability, the lift slope of the front wing needs to be shallower than that of the rear wing. This means the rear wing will have larger lift coefficient variation than the front wing when the system angle of attack is varied. Such a slope difference of the front wing and rear wing can be achieved by using smaller aspect ratio for the front wing and larger for the rear wing. This is accomplished for the present design with the front wing aspect ratio of 1/4 of the one for the rear wing. The front wing incidence is also increased to 3°, while the rear wing has 0° incidence. The fuselage is redesigned to improve the fuselage-wing interaction to reduce drag and the sensitivity of the fuselage pitching moment to angle of attack variation. Overall, the fuselage contribution to the pitching moment is large. Increasing the fuselage incidence angle to $i_f = 5°$ when the aircraft is at cruise condition of AoA 0° is beneficial to mitigate the nose down pitching moment when the AoA is $-5°$. This configuration fulfills the requirement of $C_{M\alpha} < 0$ for the range of $-5° \leq \alpha \leq 2°$, which is required for longitudinal static stability.

V. Acknowledgments

The simulations are conducted on Pegasus supercomputing system at the Center for Computational Sciences at the University of Miami.

Disclosure: The University of Miami and Dr. Gecheng Zha may receive royalties for future commercialization of the intellectual property used in this study. The University of Miami is also equity owner in CoFlow Jet, LLC, licensee of the intellectual property used in this study.

References

[1] T. S. Sugandi. Prediction of static stability in tandem wing unmanned aerial vehicle. *J. Phys: Conf. Ser.*, page 1130, 2018.

[2] G.-C. Zha and D. C. Paxton. A Novel Flow Control Method for Airfoil Performance Enhancement Using Co-Flow Jet. *Applications of Circulation Control Technologies*, Chapter 10, p. 293-314, Vol. 214, Progress in Astronautics and Aeronautics, AIAA Book Series, Editors: Joslin, R. D. and Jones, G.S., 2006.

[3] G.-C Zha and C. Paxton and A. Conley and A. Wells and B. Carroll. Effect of Injection Slot Size on High Performance Co-Flow Jet Airfoil. *AIAA Journal*, 43, 2006.

[4] G.-C. Zha and W. Gao and C. Paxton. Jet Effects on Co-Flow Jet Airfoil Performance. *AIAA Journal, No. 6*, 45:1222–1231, 2007.

[5] G.-C Zha and B. Carroll and C. Paxton and A. Conley and A. Wells. High Performance Airfoil with Co-Flow Jet Flow Control. *AIAA Journal*, 45, 2007.

[6] Wang, B.-Y. and Haddoukessouni, B. and Levy, J. and Zha, G.-C. Numerical Investigations of Injection Slot Size Effect on the Performance of Co-Flow Jet Airfoil . *AIAA Journal of Aircraft*, 45:2084–2091, 2008.

[7] B. P. E. Dano, D. Kirk, and G.-C. Zha. Experimental Investigation of Jet Mixing Mechanism of Co-Flow Jet Airfoil. AIAA Paper 2010-4421, 5th AIAA Flow Control Conference, Chicago, IL,, 28 Jun - 1 Jul 2010.

[8] B. P. E. Dano, G.-C. Zha, and M. Castillo. Experimental Study of Co-Flow Jet Airfoil Performance Enhancement Using Micro Discreet Jets. AIAA Paper 2011-0941, 49th AIAA Aerospace Sciences Meeting, Orlando, FL,, 4-7 January 2011.

[9] Lefebvre, A. and Dano, B. and Di Franzo, M. and Bartow, W. and Zha, G.-C. Performance of Co-Flow Jet Flow Airfoil with Variation of Mach Number. AIAA Paper 2013-0490, 51st AIAA Aerospace Science Meeting, Grapevine, TX, 7-10 Jan. 2013, to appear in Journal of Aircraft, 2016.

[10] Lefebvre, A. and Zha, G.-C. Numerical Simulation of Pitching Airfoil Performance Enhancement Using Co-Flow Jet Flow Control. AIAA Paper 2013-2517, 31st AIAA Applied Aerodynamics Conference, San Diego, CA, 24 - 27 June 2013.

[11] Lefebvre, A. and Zha, G.-C. . Design of High Wing Loading Compact Electric Airplane Utilizing Co-Flow Jet Flow Control. AIAA Paper 2015-0772, AIAA SciTech2015: 53nd Aerospace Sciences Meeting, Kissimmee, FL, 5-9 Jan 2015.

[12] Lefebvre, A. and Dano, B. and Bartow, W. and Di Franzo, M. and Zha, G.-C. Performance and Energy Expenditure of Co-Flow Jet Airfoil with Variation of Mach Number. *AIAA Journal of Aircraft*, 53:1757–1767, 2016.

[13] Liu, Z.-X. and Zha, G.-C. Transonic Airfoil Performance Enhancement Using Co-Flow Jet Active Flow Control. AIAA Paper 2016-3472, AIAA AVIATION 2016, 8th AIAA Flow Control Conference, Washington, D.C, June 13-17, 2016.

[14] Yang, Y.-C. and Zha, G.-C. Super-Lift Coefficient of Active Flow Control Airfoil: What Is the Limit? AIAA Paper 2017-1693, AIAA SCITECH2017, 55th AIAA Aerospace Science Meeting, Grapevine, Texas, 9-13 January 2017.

[15] G.-C. Zha, Y. Yang, Y. Ren, and B. McBreen. Super-Lift and Thrusting Airfoil of Coflow Jet Actuated by Micro-Compressors . AIAA Paper-2018-3061, AIAA AVIATION Forum 2018, 2018 Flow Control Conference, Atlanta, Georgia, June 25-29, 2018.

[16] G.-C. Zha, Yan Ren, Jiaye Gan, and Daniel Espinal. A High Efficiency Low Noise VTOL/ESTOL Concept Using CoFlow Jet Airfoil. AIAA Paper 2019-04467, AIAA Propulsion and Energy Forum, Indianapolis, Indiana, August 2019.

[17] G.-C. Zha, Y. Shen, and B. Wang. An improved low diffusion E-CUSP upwind scheme . *Journal of Computer & Fluids*, 48:214–220, 2011.

[18] B.-Y. Wang and G.-C. Zha. A General Sub-Domain Boundary Mapping Procedure For Structured Grid CFD Parallel Computation. *AIAA Journal of Aerospace Computing, Information, and Communication*, 5, No.11:2084–2091, 2008.

[19] J Boling, G.-C. Zha, and Cale Zeune. A high-speed, high-efficiency vtol concept using coflow jet airfoil. AIAA Paper 2020-2792, AIAA AVIATION 2020 FORUM, 2020.

[20] Wang, Y. and Zha, G.-C. Study of Mach Number Effect for 2D Co-Flow Jet Airfoil at Cruise Conditions. AIAA Paper 2019-3169, AIAA Aviation 2019, AIAA Applied Aerodynamics Conference, Dallas, Texas, 17-21 June 2019.